# Relative importance of initial conditions on outflows from multiple fans

K. Takamure[1,*] and S. Ozono[2]

[1]*Department of Mechanical Science and Engineering, Nagoya University, Nagoya, Japan*

[2]*Department of Mechanical Design System Engineering, University of Miyazaki, 1-1 Gakuen-Kibanadai-Nishi, Miyazaki, Japan*

(Received 25 July 2018; published 30 January 2019)

Generation of homogeneous isotropic turbulence was attempted using an innovative "multifan wind tunnel" with 99 fans installed. The driving method used is based on a principle that the shear layers generated between outflows from the adjacent ducts lead to turbulent flow downstream. First, a signal composed of two frequency components is set, and then it is fed to all the fans for three kinds of arrangements of phases. Here, parameter $N$ is introduced as the number of phases used for the 99 fans, which represents a variety of emanated shear layers. Furthermore, $S$ is introduced as a measure of shear magnitude at the inlet of the test section. Relative importance of the initial conditions ($N$ and $S$) in the development of turbulence was investigated. To estimate the contribution from naturally induced turbulence, we numerically decomposed the resulting velocity fluctuations into the periodic and nonperiodic component. Energy spectra for three values of $N$ were calculated using nonperiodic data. The inertial subrange of a gradient of $-5/3$ widens with increasing $N$. The value $S$ is the largest for $N = 2$, but the turbulence intensity of the nonperiodic component is the largest for $N = 99$. Hence, it might be suggested that the shear magnitude at the inlet of the test section is not as important as the variety of shear layers for effective generation of high-Reynolds-number turbulence.

DOI: 10.1103/PhysRevE.99.013112

## I. INTRODUCTION

The effects of initial conditions (i.e., the conditions under which the turbulence was produced) on the development of turbulence have been investigated by placing different kinds of turbulence generators at the inlet of the test section. This issue is of fundamental interest in physical understanding of turbulence as well as in engineering applications.

A rectangular passive grid [1,2] is the most classical turbulence generator. Using such a grid, approximately homogeneous isotropic turbulence (HIT) can be easily generated. Hence, even in recent years, many experiments using the static grids were conducted to get a clear picture of development of homogeneous isotropic turbulence [3–9]. However, since the turbulence Reynolds number is low without the Kolmogorov inertial subrange, it is insufficient for verification of turbulence theory.

Wind tunnel experiments on the turbulence generated by fractal grids have provided much detailed data. Hurst and Vassilicos [10] showed that fractal grids generate higher Reynolds number, probably due to increased turbulence intensity, than the conventional rectangular grids. Seoud and Vassilicos [11] showed that fractal grid turbulence does not take a constant value of turbulence energy dissipation rate toward the downstream direction. These studies provide detailed characteristics of turbulence for a certain type of grid, but it seems difficult to generalize the results to other cases, because different geometries naturally lead to different turbulence characteristics.

The passive grids can produce approximately homogeneous isotropic turbulence only with relatively moderate Reynolds numbers. Makita [12] devised an active grid and realized a high-Reynolds-number turbulence. Using a similar grid, Mydlarski and Warhaft [13] examined the high-Reynolds-number asymptotic behavior of the turbulence. Building a large wind tunnel with an active grid installed, Hearst and Lavoie [14] investigated the evolution of turbulence generated by three kinds of wing geometries. For the method using an active grid, turbulence is produced by a combination of static grid and dynamic wings. The influence of the stirring protocol on the generated turbulence was reported in Refs. [15–19].

The principle of turbulence generation using the multifan wind tunnel (MFWT) is different from that of the grid-generated turbulence. Respective fans produce outflows corresponding to the time-varying input signals. The signals are defined by frequencies, amplitudes, and phase differences. Hence, combinations of these parameters can create different turbulent flows. Ozono and Ikeda [20] assumed an input signal composed of 40 frequency components and randomly assigned 99 phases to each fan. Within a relatively short distance, high-Reynolds-number turbulence with two decades of inertial subrange was obtained, where $\mathrm{Re}_\lambda \approx 750$. Here, $\mathrm{Re}_\lambda$ is defined by $\mathrm{Re}_\lambda = u'\lambda/\nu$; $u'$ is the root-mean square (r.m.s.) value of streamwise velocity fluctuations, $\lambda$ is the Taylor microscale, and $\nu$ is the kinematic viscosity. The mode is referred to as "random-phase mode" hereafter. In some studies, using the Makita-style active grids, comparable $\mathrm{Re}_\lambda$ was achieved (e.g., Kang *et al.* [21], $\mathrm{Re}_\lambda = 716$; Larssen and Devenport [22], $\mathrm{Re}_\lambda = 1362$). Variations of the random driving mode were considered in Ref. [15] with a highest Taylor Reynolds number $\mathrm{Re}_\lambda = 200$. A stirring protocol from a

*takamure.kotaro@a.mbox.nagoya-u.ac.jp

 

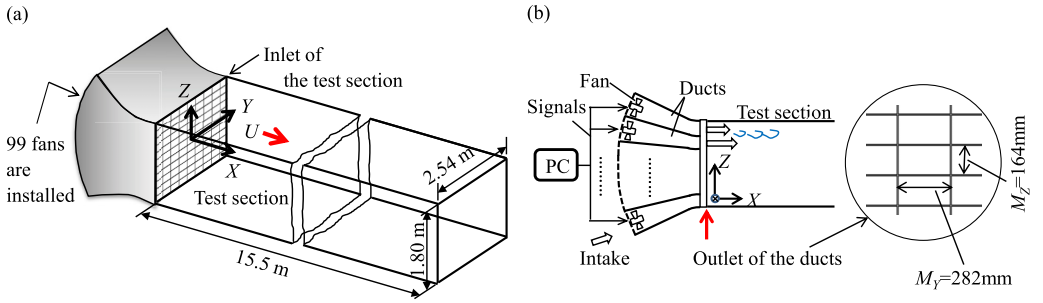


FIG. 1. Experimental setup. (a) A perspective view of the test section and the coordinate system of the multifan type wind tunnel (MFWT). (b) Side view and driving mechanism of the MFWT.

stochastic model in Ref. [18] resulted in a very large Reynolds number ($\mathrm{Re}_\lambda \approx 2000$). The response to periodic stirring with $\mathrm{Re}_\lambda \approx 500$ was studied in Ref. [17], while a stirring protocol derived from a turbulence model gave a largest $\mathrm{Re}_\lambda \approx 900$ [19].

To identify the minimum number of frequency components required to promote efficient turbulent development, we applied the random-phase mode with an input signal composed of two frequency components. The two frequencies are defined as $f_1 = n_1 f_0$ and $f_2 = n_2 f_0$, where $f_0$ is the basic frequency and $n_1$ and $n_2$ mutually prime [23]. It was confirmed that the evolution of turbulence to equilibrium was relatively slow, but in sufficiently downstream region, the measurements show characteristics of fully developed turbulence ($\mathrm{Re}_\lambda \approx 750$) similar to the case using 40 frequency components [20].

In the present study, we use three kinds of arrangements of phases, i.e., $N = 2,\ 3$, and 99, where $N$ indicates the number of phases used for the 99 fans. Furthermore, $S$ is introduced as a measure of shear magnitude based on the spatiotemporal average of velocity differences of adjacent outflows. Relative importance of the initial conditions (i.e., $N$ and $S$) in the development of turbulence is investigated.

## II. EXPERIMENTAL APPARATUS AND METHODS

### A. Experimental apparatus

A schematic of the MFWT in the University of Miyazaki is shown in Fig. 1 [24,25]. Experiments are conducted in the MFWT, which has a test section with a cross-section of 1.80 m × 2.54 m and a length of 15.5 m. This tunnel is equipped with an array of 99 small fans (9 columns × 11 rows) whose diameter is 276 mm. The fans are directly connected to AC 200V servomotors, and the rotation rate can be controlled individually via a single personal computer. The airflow generated by the fans passes through ducts with the contraction ratio 1 : 1.8, and honeycombs (212 mm in length and 30 mm in diameter), and is finally discharged into the test section. If the velocities from the adjacent ducts are different, shear layers are expected to develop and interact each other. This should lead to evolution of turbulence. As shown in Fig. 1(b), the sizes at the exit of the ducts are $M_Y = 282$ mm in width and $M_Z = 164$ mm in height. The thickness of the duct walls is 3 mm, which is much smaller than $M_Y$ and $M_Z$.

The origin of the coordinate system is the center of the test section, and the flow velocities ($U + u$, $v$, $w$) are in the streamwise ($X$), spanwise ($Y$), and vertical ($Z$) direction, respectively. Here, $U$ is the mean velocity and $u$, $v$, and $w$ are the velocity fluctuations. Measurement positions are represented in a nondimensional form as ($X/M_D$, $Y/M_Y$, $Z/M_Z$), where $M_D = (M_Y \times M_Z)^{1/2} = 215$ mm.

Measurements of instantaneous velocity are made with a constant-temperature hot-wire anemometer (KANOMAX, System-7000). X-wire probes (Model-1241) or I-wire probes (Model-1210) are mounted on a traverser, which is used to shift the sensors to a required position. The data are sampled at a frequency of 5 kHz, with an analog cutoff filter at 2 kHz. The diameter of the wires is nominally 5.0 $\mu$m and the sensing length $l = 1.0$ mm. The Taylor scale $\lambda$ and the Kolmogorov length scale $\eta$ are 13 and 0.31 mm, respectively. Thus, our measurements resolve to around 3 $\eta$. Spectra shown in Figs. 8 and 12 are estimated by taking arithmetic means over 54 spectra obtained from the sampling number of 204 800. To estimate the uncertainty of hot-wire anemometry, we used a conventional method including the $t$ test. Recently, the uncertainty was systematically assessed [26]. Further study in this direction might be required for the future.

### B. Input signals and driving methods

The input signal used is composed of two frequency components as follows:

$$u_{\mathrm{in}} = u'_{\mathrm{in}}(\sin 2\pi f_1 t + \sin 2\pi f_2 t) + U_{\mathrm{in}}, \tag{1}$$

where $u'_{\mathrm{in}}$ is the r.m.s. value of the input signal and set to $u'_{\mathrm{in}} = 1$ m/s. Note that the subscript "in" denotes the input signal. The mean streamwise velocity is set to $U_{in} = 4.67$ m/s, so that the total flow rate of the cross section is 21.4 $\mathrm{m}^3$/s in any case.

The frequencies of the input signal used in the present study were determined to satisfy the following limit. In a preliminary experiment, we examined a frequency response of the wind tunnel by using a sinusoidal signal, where the response is defined by the ratio of the measured amplitude (output) to the input one. It is found that for frequencies beyond 1 Hz, the response decays considerably. Thus 0.72 Hz is selected as the higher frequency $f_2$. According to a study by Gotoh and Watanabe [27], energy transfer by the interaction between eddies of different scales occurs particularly for a scale ratio around 2. Hence, the lower frequency $f_1$ is set to 0.36 Hz.

First, integers are assigned to all the fans as shown in Figs. 2. Hence, the input signals are given as follows:

$$u_{\mathrm{in}}(t) \Longrightarrow u_{\mathrm{in}}(t + \psi_n) \quad (n = 1, \ldots, N), \tag{2}$$

(a)

| | | | | | | | | |
|---|---|---|---|---|---|---|---|---|
| 1 | 2 | 1 | 2 | 1 | 2 | 1 | 2 | 1 |
| 2 | 1 | 2 | 1 | 2 | 1 | 2 | 1 | 2 |
| 1 | 2 | 1 | 2 | 1 | 2 | 1 | 2 | 1 |
| 2 | 1 | 2 | 1 | 2 | 1 | 2 | 1 | 2 |
| 1 | 2 | 1 | 2 | 1 | 2 | 1 | 2 | 1 |
| 2 | 1 | 2 | 1 | 2 | 1 | 2 | 1 | 2 |
| 1 | 2 | 1 | 2 | 1 | 2 | 1 | 2 | 1 |
| 2 | 1 | 2 | 1 | 2 | 1 | 2 | 1 | 2 |
| 1 | 2 | 1 | 2 | 1 | 2 | 1 | 2 | 1 |
| 2 | 1 | 2 | 1 | 2 | 1 | 2 | 1 | 2 |
| 1 | 2 | 1 | 2 | 1 | 2 | 1 | 2 | 1 |

(b)

| | | | | | | | | |
|---|---|---|---|---|---|---|---|---|
| 1 | 2 | 3 | 4 | 5 | 1 | 2 | 3 | 4 |
| 4 | 5 | 1 | 2 | 3 | 4 | 5 | 1 | 2 |
| 2 | 3 | 4 | 5 | 1 | 2 | 3 | 4 | 5 |
| 5 | 1 | 2 | 3 | 4 | 5 | 1 | 2 | 3 |
| 3 | 4 | 5 | 1 | 2 | 3 | 4 | 5 | 1 |
| 1 | 2 | 3 | 4 | 5 | 1 | 2 | 3 | 4 |
| 4 | 5 | 1 | 2 | 3 | 4 | 5 | 1 | 2 |
| 2 | 3 | 4 | 5 | 1 | 2 | 3 | 4 | 5 |
| 5 | 1 | 2 | 3 | 4 | 5 | 1 | 2 | 3 |
| 3 | 4 | 5 | 1 | 2 | 3 | 4 | 5 | 1 |
| 1 | 2 | 3 | 4 | 5 | 1 | 2 | 3 | 4 |

(c)

| | | | | | | | | |
|---|---|---|---|---|---|---|---|---|
| 57 | 31 | 6 | 37 | 13 | 30 | 97 | 93 | 59 |
| 99 | 2 | 98 | 77 | 84 | 72 | 22 | 15 | 79 |
| 78 | 44 | 95 | 63 | 58 | 69 | 26 | 16 | 3 |
| 56 | 53 | 24 | 86 | 41 | 54 | 40 | 1 | 52 |
| 92 | 75 | 60 | 64 | 28 | 25 | 89 | 47 | 62 |
| 50 | 67 | 66 | 12 | 55 | 65 | 81 | 38 | 70 |
| 5 | 61 | 33 | 87 | 96 | 42 | 35 | 51 | 34 |
| 19 | 74 | 83 | 36 | 45 | 21 | 11 | 80 | 27 |
| 32 | 82 | 73 | 8 | 18 | 71 | 46 | 29 | 17 |
| 14 | 49 | 85 | 48 | 10 | 90 | 23 | 9 | 43 |
| 76 | 88 | 39 | 4 | 91 | 20 | 94 | 68 | 7 |

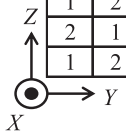


FIG. 2. Arrangement of $n$ and the coordinate axes. (a) $N = 2$, (b) $N = 5$, (c) $N = 99$.

where the phases are defined by $\psi_n = (n-1) \times T_0/N$. Here, $T_0$ is the period of the lowest frequency component among the waves involved in the input signal. For this experiment, $T_0 = 1/f_1 = 2.78$ s. $N$ is the total number of the phases used.

We examined three kinds of arrangements of phases ($N = 2,\ 5$, and 99). They are shown in a matrix form in Fig. 2. To determine how to assign integers $n$ to every fan, we make two general rules:

*Rule 1:* A set of integers from 1 to $N$ are arranged, in which no restrictions are imposed on the order. Random arrangement is permitted. For instance, in the case of $N = 5$, (2,1,3,4,5), (2,5,3,1,4), etc. are possible. The $N$-sequence is periodically repeated until the total number of integers reaches 99. Therefore, $N$ is the period of the 99-sequence.

*Rule 2:* A partial sequence with nine elements is selected from the above sequence, and is substituted into the matrix row by row so that all adjacent numbers should be different horizontally and vertically.

The two rules are introduced to determine an arrangement of $n$ as automatically as possible. By Rule 1, two-dimensional array of $n$ is reduced to one-dimensional sequence, and thereby parameter $N$ can be defined. According to $N$, in the present paper, three sequences are given as follows:

$$1, 2, 1, 2, 1, 2, \ldots \quad (\text{for } N = 2), \tag{3a}$$

$$1, 2, 3, 4, 5, 1, 2, 3, \ldots \quad (\text{for } N = 5), \tag{3b}$$

$$57, 31, 6 \ldots \ 94, 68, 7 \quad (\text{for } N = 99). \tag{3c}$$

The case $N = 99$ does not seem to be periodic, but can be interpreted as a period of 99. Rule 2 provides the way to satisfy the condition that all adjacent numbers should be different horizontally and vertically, which is essential to produce shear layers. To satisfy Rule 2, for $N = 2$ and 5, the way of assigning is not automatic, but the condition can be satisfied by a suitable shift row by row. For $N = 2$, the signals of adjacent fans are out of phase with each other. A sequence for the $N = 99$ case is obtained from a random number generator of PC, and an arrangement of 99 integers can be determined automatically by assigning the sequence from the upper left to lower right.

Parameter $N$ does not uniquely determine "variety" of shear layers. At present, we have no theory available to quantify "variety" of an array of numbers as shown in Fig. 2. Since large $N$ indicates many different states of shear layers are injected, it should be reasonable to say that a flow state with larger $N$ has more variety.

Figure 3 illustrates the relationship between the input signals (right) and the shear layers (left) generated at the outlet of the ducts. The two input signals are fed to two adjacent fans, Fan1 and Fan2. Although the two input signals have the same waveform, they are shifted by a phase $\psi_n$. Hence, at a time $t$, a difference in outflow velocity occurs between ①and ②. The two signals cause instantaneous velocities $u_1$ and $u_2$ at the outlet, and then the difference $\delta(t) = u_1 - u_2$ leads to a shear layer.

Here, we attempt to estimate quantitatively the magnitude of shears. In a planar mixing layer between two fluids flow, $\delta/\nu$, i.e., the Reynolds number per unit length, has been used as a parameter [28]. In the present experiment, $\nu$ is neglected since a single fluid is used. To specify the global state of shears, we introduce the shear magnitude $S$ as follows:

$$S = \frac{1}{UT_0 \sum \partial M_k} \sum_{k \in \text{Bnd}} \partial M_k \int_0^{T_o} |\delta_k(t)| dt, \tag{4}$$

where $\partial M_k$ denotes the boundary lengths at the outlet of a duct (i.e., $M_y$ and $M_z$) and "$k \in$ Bnd" indicates the sum over all the boundaries, except for those along the tunnel walls.

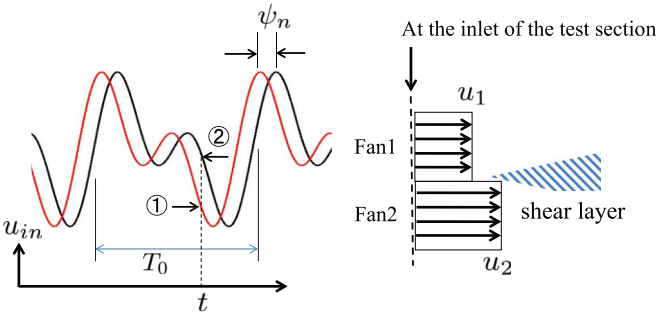


FIG. 3. Sketch of the mechanism of generating unsteady shears. Assume two signals shifted by $\psi_n$ are fed to two fans, named Fan1 and Fan2. At a time $t$, a difference in velocity occurs. This difference leads to a difference between blowing velocities $u_1$ and $u_2$, thereby causing a shear layer.

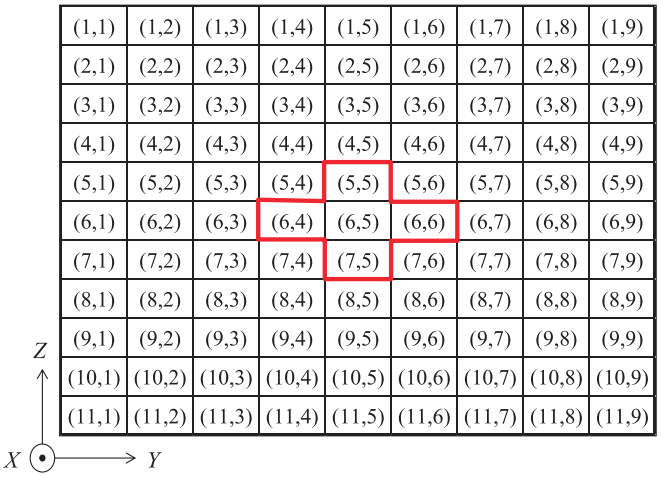


FIG. 4. Indices assigned to each fan. The region surrounded by a red line shows the range used for estimating $S_c$. Here, $S_c$ is introduced to confirm whether the local shear magnitude around the central duct is close to the average shear magnitude. The indices correspond to $(i, j)$ of Eqs. (A1) and (A2) in the Appendix.

Since the velocity difference $\delta$ depends on the boundaries, the subscript $k$ is used as $\delta_k$. Equation (4) is a nondimensional form of the spatiotemporal integral of the velocity differences between adjacent outflows.

Since measurements are conducted mainly along the centerline of the wind tunnel, the results might be influenced by local upstream conditions around the central duct. Therefore, the local shear magnitude around the central duct should be comparable to the shear magnitude over the cross section. $S_c$ is defined similarly to Eq. (4):

$$S_c = \frac{1}{UT_0 \sum \partial M_k} \sum_{k\in\text{Local}} \partial M_k \int_0^{T_o} |\delta_k(t)| dt. \tag{5}$$

$S_c$ means the local magnitude of shear generated between a central duct [(6,5) in Fig. 4] and four adjacent ducts around it. "$k \in$ Local" indicates the sum over four boundaries.

The results of Eqs. (4) and (5) are shown in Table I. The local value $S_c$ is close to the global average value $S$ for any $N$. Therefore, the present results cannot be attributed to the extremely biased (i.e., much larger or smaller than the average) local shear magnitude. For the case of $N = 99$, we examined seven kinds of different combinations other than the combination shown in Fig. 2(c). It was confirmed that $S$ and $S_c$ fall within the range of $20.8 \leqslant S \leqslant 21.5$ and $19.2 \leqslant Sc \leqslant 22.5$, which shows a $\pm 2\%$ variation in $S$ and $S_c$. For details of Eqs. (4) and (5), see the Appendix.

TABLE I. Comparison between $S$ and $S_c$ for each $N$. $S$ and $S_c$ are defined by Eqs. (4) and (5), respectively. $S$ represents the shear magnitude averaged over the cross section at the inlet, while $S_c$ the local one.

| $N$ | $S$ | $S_c$ |
|---|---|---|
| 2 | 30.4 | 30.4 |
| 5 | 26.1 | 25.9 |
| 99 | 21.3 | 21.5 |

## III. RESULTS

### A. Characteristics of raw data

In this section, we examine the evolution of turbulence characteristics using raw data. For each case of $N = 2$, 5, and 99, the vertical profile of mean velocity $U$ at $Y/M_Y = 0$ is presented at some downstream distances in Fig. 5(a). In the central core region ($3.0 \leqslant Z/M_Z \leqslant 8.0$), the inhomogeneity of mean velocity is 3% at $X/M_D = 37.2$ and 2% at $X/M_D = 51.2$. Here, the inhomogeneity is defined as $\max|(a_i - a_0)/a_0|$, where $a_i$ is some physical value at any position and $a_0$ is the averaged value over $a_i$. Vertical homogeneity is found to be acceptable for $X/M_D \geqslant 37.2$. Figure 5(b) shows the variation of the streamwise mean velocity along the centerline of the tunnel. The estimates of the measurement uncertainties are provided as error bars and are calculated for the 95% confidence interval. The error bars are almost invisible for $X/M_D > 20$, since the uncertainty is contained within the symbol size. The test section of the MFWT has no gradient of the walls in the downstream direction. For such a wind tunnel, in general, the streamwise mean velocity in the core region is somewhat accelerated owing to growth of boundary layers on the walls. This probably holds true for the present case. However, the acceleration is small enough for $X/M_D > 40$.

The time traces of streamwise velocity measured at the farthest downstream location ($X/M_D = 60.5$) are shown along with that of the input signal in Fig. 6(a). In the analysis, the input time trace is shifted until the cross-correlation coefficient between the input and measured one reaches the highest [Fig. 6(b)]. Here, the cross-correlation coefficient $C(\Delta t)$ is defined as

$$C(\Delta t) = \frac{\overline{u_{\text{in}}(t)u(t+\Delta t)}}{\overline{u(t)^2}}, \tag{6}$$

where $\Delta t$ is the time-lag. The correlation peaks appear at intervals of $\Delta t = 1/f_1 = 2.78$ s. The peak values of $N = 2$, 5, and 99 are 0.48, 0.35, and 0.18, respectively [indicated by arrows in Fig. 6(b)], thus indicating the time traces are better correlated, as $N$ decreases. For $N = 2$, fine-scale fluctuations are less apparent, and it appears that large-scale periodicity remains. As the number of phases $N$ increases (i.e., $N = 5$ and 99), fine-scale fluctuations in the measurements are amplified, thus suggesting that the transition to turbulence is promoted.

The streamwise evolution of the ratio $u'/v'$, as a measure of anisotropy, is presented in Fig. 7, where error bars are shown. Immediately downstream of the inlet of the test section, the range of the error bars is relatively large, but for $X/M_D > 20$ it was at most 4% of the average for any $N$. The isotropy ratio $u'/v'$ decreases rapidly with downstream distance, and it remains roughly constant from $X/M_D = 40$. Comparing $u'/v'$ at the farthest downstream location (i.e., $X/M_D = 60.5$), $u'/v'$ is closer to unity with increasing $N$. The case of $N = 2$ shows a large anisotropy of $u'/v' = 3.2$. This relatively large value should result from the persistent wave, which originates from forcing as observed in the time trace (Fig. 6).

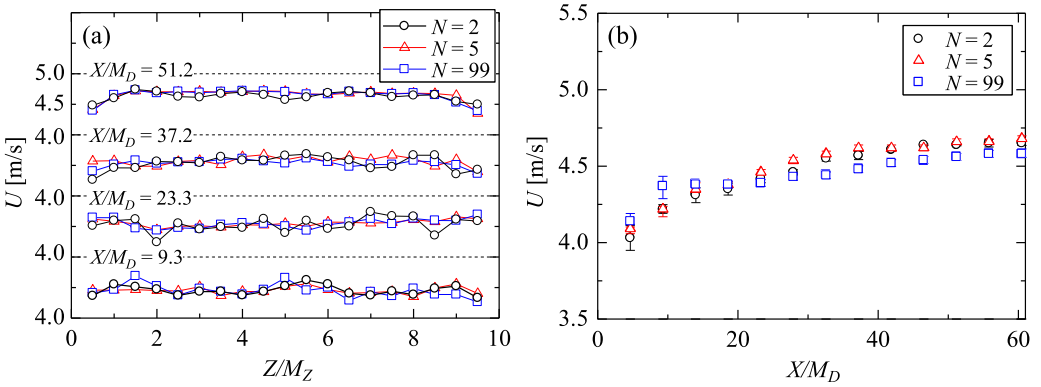


FIG. 5. Spatial variations of average velocity $U$. (a) Vertical variations. (b) Streamwise variations.

The black lines in Fig. 8 show power spectra of the streamwise velocity fluctuation calculated from the raw data at $X/M_D = 60.5$. There are numerous peaks for the three cases of $N$ ($N = 2$, 5, 99). Some studies pointed out that when forcing with two frequencies $f_1$ and $f_2$ are applied to a flow, the turbulent energy will be transported to linear combinations of $f_1$ and $f_2$, $\alpha f_1 + \beta f_2$, where $\alpha$ and $\beta$ are integers [29,30]. Therefore, when two frequencies of forcing are related by $f_2 = 2f_1$, energy would be transported to frequencies that are integral multiples of $f_1$. It is evident from Fig. 8 that most peaks at lower frequencies are multiples of $f_1$.

It is found that as $N$ increases, fine-scale fluctuations were more pronounced (Fig. 6), and the isotropy was more improved (Fig. 7). From the power spectra in Fig. 8, however, numerous sharp peaks were observed. It was confirmed that the frequencies corresponding to the peaks were integral multiples of $f_1$. Evidently, the periodic components, which originates from the input, remain even sufficiently downstream. Thus, of primary interest is the way in which the relative contribution of nonperiodic components to the total turbulence kinetic energy varies with downstream distance.

### B. Partition of turbulent kinetic energy

In this section, we examine how the characteristics of nonperiodic components change with $N$, by eliminating periodic components from the raw data. The streamwise velocity fluctuation $u$ is assumed to be decomposed as follows:

$$u = u_\theta + u_s, \tag{7}$$

where $u_\theta$ and $u_s$ are the periodic and the nonperiodic components, respectively. For the purpose of facilitating decomposition of periodic and nonperiodic components, we selected the two frequencies $f_1$ and $f_2$ satisfying the relation $2f_1 = f_2$, and thereby the fine peaks can be conveniently identified. The decomposition was conducted by the following method. First, Fourier components are calculated with a fast Fourier transform (FFT). Next, the Fourier components at integral multiples of $f_1$ were eliminated. The peak values were replaced by linearly interpolated values to make a smooth Fourier spectral curve. Finally, inverse Fourier transform of this spectrum yielded a reduced time trace, where periodic components are eliminated. When $v$ was also decomposed using the same procedure, the periodic components of $v$ were much smaller than the nonperiodic one. Therefore, the raw data were used in its original form.

The power spectra estimated by using the reduced time trace are shown by red lines in Fig. 8. It is evident that the input frequency components and their harmonics are removed. An example of decomposition in time domain is shown in Fig. 9. Evidently, the nonperiodic component $u_s$

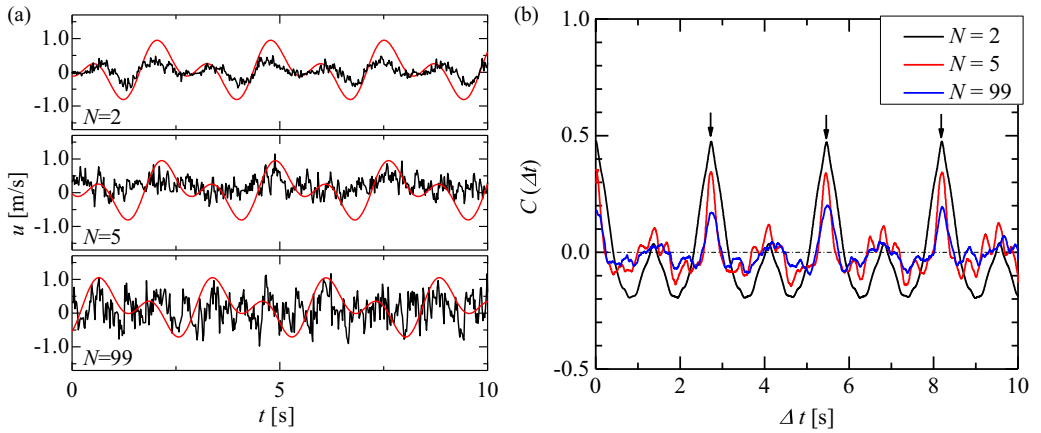


FIG. 6. (a) Comparison of the time traces of velocity fluctuations $u$(black) at $X/M_D = 60.5$ and $Y/M_Y = Z/M_Z = 0$ with the input signal $u_{\text{in}}$(red). (b) Cross-correlation coefficient of the input signal and the turbulent velocity at $X/M_D = 60.5$. As the input signal is shifted in phase, the correlation coefficient reaches a maximum [indicated by the arrow in Fig. 6(b)], when the signal is fixed and displayed in the Fig. 6(a).

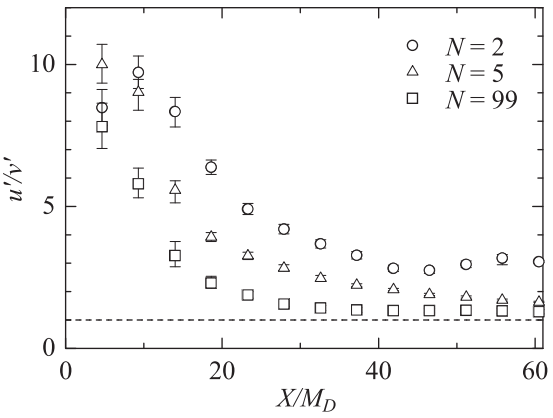


FIG. 7. Streamwise development of anisotropy.

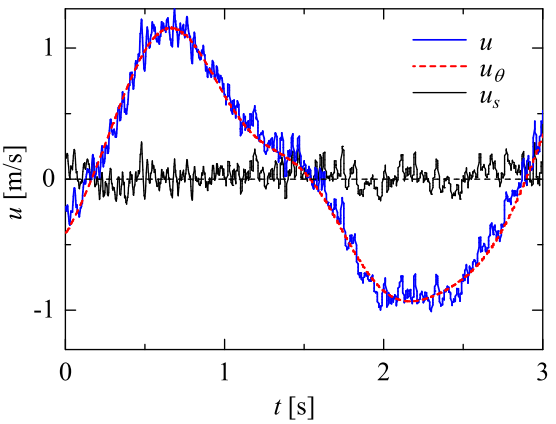


FIG. 9. Typical example of decomposition of $u$ into $u_\theta$ and $u_s$. A time trace $u$ is taken from data for $N = 2$ at $X/M_D = 4.6$. An extracted component $u_s$ seems to fluctuate about a level of $u = 0\,\mathrm{m/s}$.

seems to fluctuate about a level denoting $u = 0\,\mathrm{m/s}$, with periodic components eliminated. From these results (Figs. 8 and 9), indicating the proposed numerical analysis using FFT transform is valid for the decomposition.

Figure 10(a) shows the streamwise variation of turbulence intensity, $u_s'/U$ and $v'/U$. Here, $u_s'$ shows the r.m.s. values of $u_s$. For any $N$, beyond a broad maximum at $X/M_D \approx 20 - 40$, both $u_s'/U$ and $v'/U$ decay downstream monotonically. Comparing intensity for different $N$ at a fixed downstream location, both $u_s'/U$ and $v'/U$ become larger with increasing $N$.

Using $u_s'$, a modified isotropy ratio $u_s'/v$ can be defined. Figure 10(b) shows the streamwise variation of $u_s'/v'$, where error bars are included. Except for a region close to the inlet of the test section, the measurement uncertainty is very small. For $N = 5$ and 99, the isotropy ratio asymptotes to approximately 1.1 at the farthest downstream region, while for $N = 2$ somewhat undulation is perceived for $X/M_D > 30$.

The turbulence Reynolds number for $u_s$ is defined by

$$\mathrm{Re}_{\lambda s} = \frac{u_s'\lambda}{\nu}. \tag{8}$$

Here, $\lambda$ is the Taylor's microscale and it is calculated by

$$\lambda^2 = U^2 u_s'^2 \Big/ \overline{\left(\frac{\partial u_s}{\partial t}\right)^2}, \tag{9}$$

where Taylor's hypothesis is used, and the overbar denotes the time average. Figure 11 shows the streamwise variation of the turbulence Reynolds number $\mathrm{Re}_{\lambda s}$. Figure 5(b) shows the mean velocity significantly changes at upstream region, but it is relatively constant for $X/M_D > 40$. Hence, the estimate using Taylor's hypothesis is valid for $X/M_D > 40$. It should be worth pointing out that the turbulence Reynolds number increases with increasing $N$, for a fixed downstream location.

Figure 12 shows the energy spectra for $u_s$. The energy spectra $E(k)$ and the wave number $k$ are nondimensionalized by the energy unit $(\epsilon\nu^5)^{1/4}$ and $\eta$, respectively. Here, the energy dissipation rate $\epsilon$ is calculated on the assumption of local isotropy, as follows:

$$\epsilon = \frac{15\nu u_s'^2}{\lambda^2}. \tag{10}$$

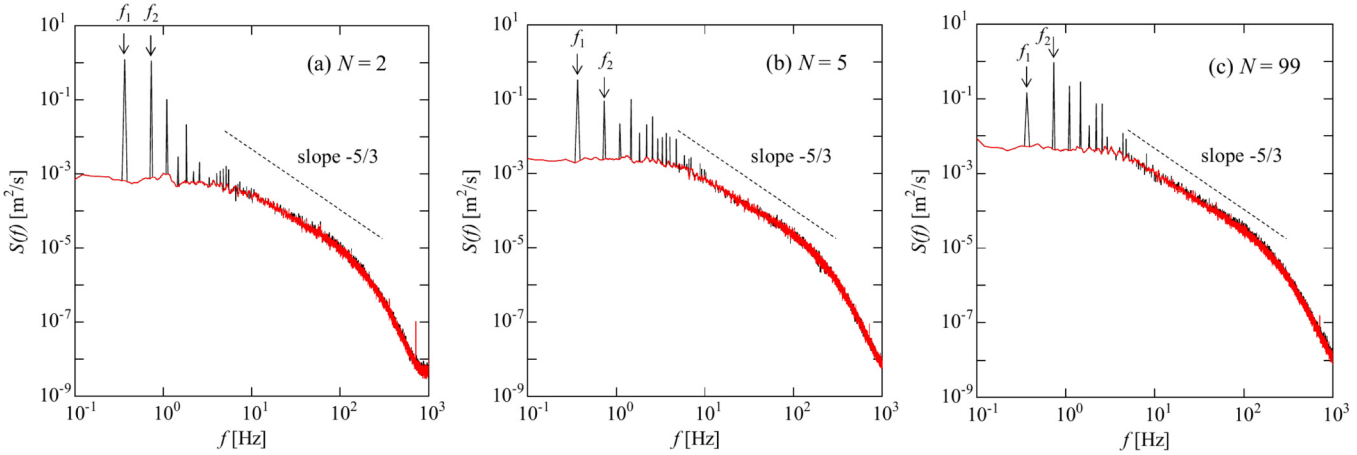


FIG. 8. Comparison of power spectra of the streamwise velocity fluctuation at $X/M_D = 60.5$. (a) $N = 2$, (b) $N = 5$, (c) $N = 99$. The black line is from the raw data, and the red line is obtained by removing the peaks.

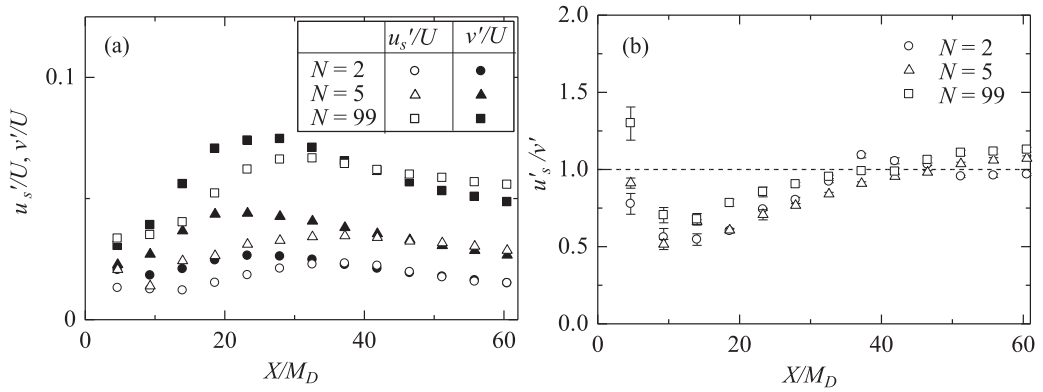


FIG. 10. Characteristics of $u_s'$. (a) Streamwise variation of intensity. (b) Streamwise variation of isotropy.

From Fig. 12, these energy spectra collapse in the region with a slope of $-5/3$ corresponding to Kolmogorov's inertial subrange. The inertial subrange extends more widely to lower wave numbers, as $N$ increases. In other words, the forcing energy is transported from the input wave numbers to a wider range of wave numbers, as $N$ increases.

Comparing the peak values at input frequencies $f_1$ and $f_2$ in Fig. 8, the values for $N = 2$ is appreciably larger than those of $N = 5$ and 99. This means the periodic components, which originate from forcing, persist far downstream. Thus, it is expected that the energy transfer from the forcing to the nonperiodic components is significantly less for $N = 2$ than for the other cases. This is supported by the fact that the intensity of $N = 2$ is smaller than those of $N = 5$ and 99, as shown in Fig. 10(a).

Figures 10 and 12 indicate that as $N$ becomes larger, turbulence develops more fully in the far downstream region. Here, the "fully developed turbulence" means the flow composed of a wide range of length scales, from the integral scale to Kolmogorov's microscale.

Further insight into the development of turbulence might be gained by examining the streamwise change in the contribution of the periodic and nonperiodic components. Since we define $u(t)$ as $u_\theta + u_s$ [i.e., Eq. (7)], the kinetic energy can be decomposed as follows:

$$\langle u^2 \rangle = \langle (u_\theta + u_s)^2 \rangle = \langle u_\theta^2 \rangle + 2\langle u_\theta u_s \rangle + \langle u_s^2 \rangle. \qquad (11)$$

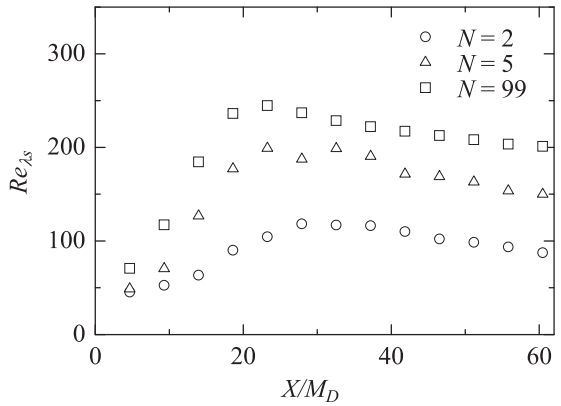


FIG. 11. Streamwise variation of the Taylor-microscale Reynolds number $\mathrm{Re}_{\lambda s}$.

We confirmed that the cross term $2\langle u_\theta u_s \rangle$ becomes sufficiently small relative to other terms for $X/M_D > 30$ downstream as shown in Fig. 14. Hence, it does not affect the subsequent discussion.

Figure 13 shows the streamwise variation of the turbulence kinetic energy, $q^2 = u'^2 + v'^2 + w'^2$, and the periodic components, $u_\theta'^2$. Here, we estimated the turbulent energy by using $q^2 = u'^2 + 2v'^2$ on the assumption of axial symmetry. The difference between $q^2$ and $u_\theta'^2$ is nearly equal to the total energy of nonperiodic components, i.e., $u_s'^2 + v'^2 + w'^2$. In the figure, this difference corresponds to the width between solid and open symbols. Comparing the differences for the three cases of $N$ at a fixed location, we can find that the difference widens with increasing $N$ at least for $X/M_D > 20$. This supports the view that turbulence develops more rapidly with increasing $N$.

As seen in Fig. 13, the turbulent energy decays to a small value, so that the partition of energy becomes unclear. To show it more clearly, a stacked bar chart normalized by the total energy is employed in Fig. 14. For all the cases of $N$, $u_\theta'^2$ decreases downstream, but, by contrast, $u_s'^2$ increases. For $N = 2$, $u_\theta'^2$ persists and occupies a substantial part even farthest downstream, but for $N = 5$ and 99, the periodic component

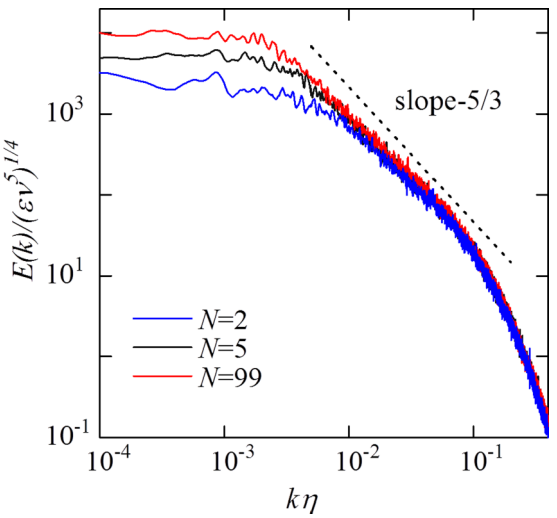


FIG. 12. Comparison of energy spectra at $X/M_D = 60.5$. Nonperiodic data $u_s$ are used in the analysis.

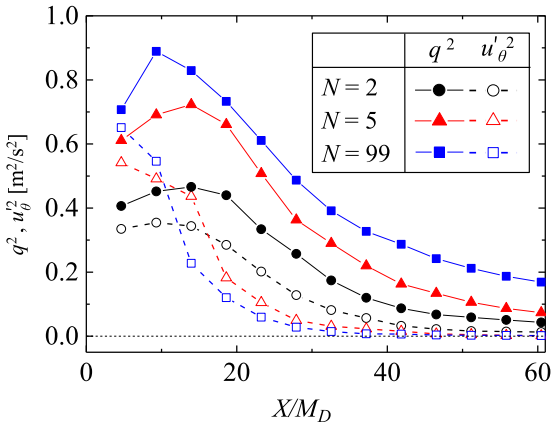


FIG. 13. Streamwise variation of $u_\theta'^2$ and $q^2$. The difference between $q^2$ and $u_\theta'^2$ is nearly equal to the total energy of nonperiodic components, i.e., $u_s'^2 + v'^2 + w'^2$.

$u_\theta'^2$ rapidly decays. Also visible is a feature common to $N = 5$ and 99 in Fig. 14. The sum of $u_s'^2$ and $u_\theta'^2$ stays almost constant for $X/M_D > 20$. This indicates the exchange of energy between $u_s'^2$ and $u_\theta'^2$, while balancing energy ratios in each direction. The periodic component is mainly transferred to the nonperiodic component for $X/M_D > 20$, and an increase in $N$ promotes the energy exchange. Furthermore, Fig. 14 suggests that a simple sinusoidal forcing of relatively small amplitude plays a role of "marker," which indicates an extent the influence of initial conditions reaches.

For the case of $N = 2$, the signals from any pair of the adjacent fans are out of phase with each other, as shown in Fig. 2(a). According to Table I, the shear amplitude $S$ for $N = 2$ is 16% larger than that for $N = 5$, and 43% larger than that for $N = 99$. If the energy transfer from the periodic to the nonperiodic component depends only on the shear amplitude $S$ at the inlet, the case of $N = 2$ will be the most effective for turbulent development. However, as shown in Figs. 10 and 12, the transfer from periodic to nonperiodic component increases with increasing $N$. This suggests that what is important for effective development of turbulence is "variety" of shear layers rather than "amplitude" of shear at the inlet.

From the more enhanced development of turbulence for larger $N$, we infer the flow dynamics immediately downstream of the inlet. For the case of $N = 2$, the velocity difference $\delta$ between the outflows from the adjacent ducts has only one kind of functional form (sign is not considered), because the outflows from the adjacent ducts are all out of phase with each other. However, as $N$ increases, the velocity difference could have many kinds of functional forms, which implies that a large number of different shear layers are discharged into the flow.

For the case of $N = 99$, $\delta(t)$ differs from one duct boundary to another. Additionally, the velocity differences are time-varying. Therefore, the shear layers could have various strengths from various positions in a variety of directions at the inlet. Initially, these shear layers lead to a number of laminar vortices, probably due to the pairing of eddies caused by K-H instability [28], or interaction between two shear layers that can be seen in the wake of bluff bodies. While convecting downstream, the vortices evolve into turbulence, as they interact and mingle. For grid-generated turbulence, shear layers which peel off the bars are of similar strength. Hence, the resulting eddies are generally of a single scale. However, the random-phase driving mode proposed here could create a wide variety of eddy scales from the initial. This may contribute to the effective development of turbulence.

## IV. CONCLUSIONS

Generation of homogeneous isotropic turbulence was attempted using an innovative "multifan wind tunnel" with 99 fans installed. First, a signal composed of two frequency components is assumed and then fed to all the fans for three kinds of arrangements of phases. Here, parameter $N$ is introduced as the number of phases used for the 99 fans, which represents variety of emanated shear layers. Furthermore, $S$ is introduced as a measure of shear magnitude at the inlet of the test section.

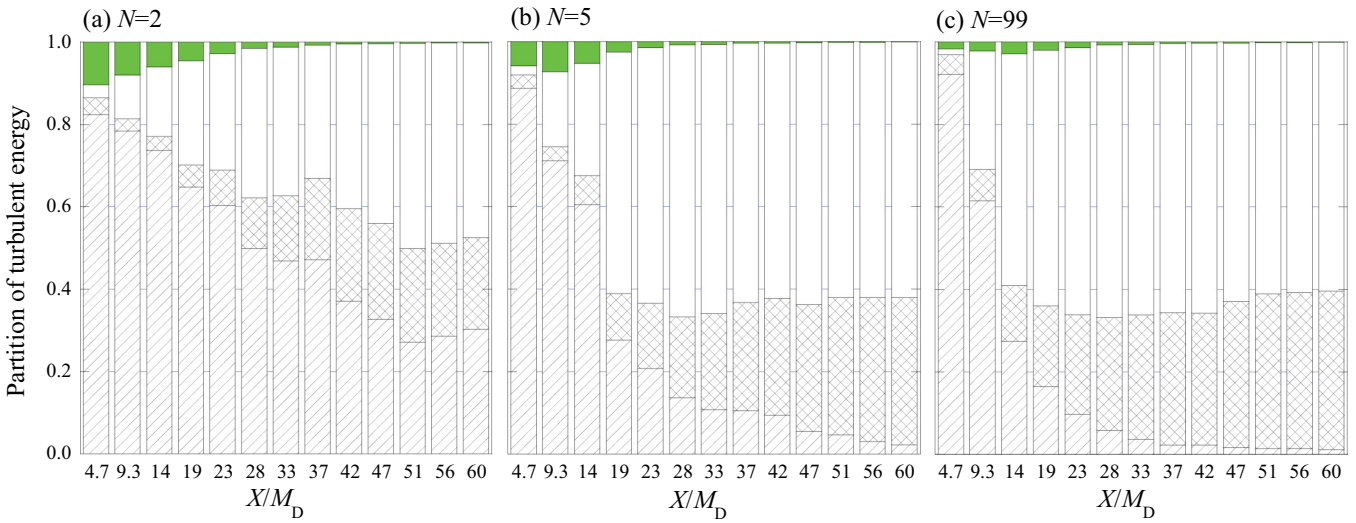


FIG. 14. Partition of turbulent energy. Hatched region, $u_\theta'^2$; cross-hatched, $u_s'^2$; white, $v'^2$ and $w'^2$; green, $2\langle u_\theta u_s \rangle$.

The relative importance of the initial conditions ($N$ and $S$) in the development of turbulence was investigated.

(i) The input signal and its corresponding time trace measured downstream were compared. As $N$ increases, fine-scale fluctuations in the trace are amplified, thus suggesting that the transition to turbulence is promoted.

(ii) Measured time traces were decomposed into periodic component $u_\theta$, and nonperiodic component $u_s$ by a numerical analysis using the Fourier transform. Using only nonperiodic component, we re-estimated turbulence intensity and spectrum, and found that the modified spectrum make the inertial subrange wider as $N$ becomes larger.

(iii) Although the shear amplitude $S$ defined at the inlet of the test section is the largest when $N = 2$, the turbulence intensity and the width of the inertial subrange of power spectrum in the nonperiodic component are the largest for $N = 99$. This result suggests that what is important for effective generation of mature turbulence is spatiotemporal "variety" of shear layers rather than "amplitude" of shear at the inlet.

## APPENDIX

The detail of the shear amplitude $S$ defined by Eq. (4) is as follows:

$$S = \frac{1}{(N_z M_z + N_y M_y) U T_0}\left[ N_z M_z \sum_{i=1}^{11}\sum_{j=1}^{8}\int_0^{T_o} |u_{in}(i, j+1) - u_{in}(i, j)|dt + N_y M_y \sum_{i=1}^{10}\sum_{j=1}^{9}\int_0^{T_0} |u_{in}(i+1, j) - u_{in}(i, j)|dt \right]. \tag{A1}$$

Here, $N_y$ and $N_z$ show the number of boundaries of ducts for $y$ and $z$ directions, respectively ($N_y = 90$, $N_z = 88$). The indices $i$, $j$ in the above equation corresponds to $(i, j)$ in Fig. 4. $S$ shows the spatiotemporal average of the differences between adjacent outflow velocities over all boundaries at the outlet of the ducts.

Details of the local shear $S_c$ occurring around the central duct defined by Eq. (5) are as follows:

$$S_c = \frac{1}{(2M_z + 2M_y) U T_0}\left[ M_y \int_0^{T_0} |u_{in}(6, 5) - u_{in}(5, 5)|dt + M_z \int_0^{T_0} |u_{in}(6, 5) - u_{in}(6, 4)|dt \right.$$
$$\left. + M_y \int_0^{T_0} |u_{in}(7, 5) - u_{in}(6, 5)|dt + M_z \int_0^{T_0} |u_{in}(6, 6) - u_{in}(6, 5)|dt \right]. \tag{A2}$$

$S_c$ shows the spatiotemporal average of the velocity differences between the central fan and the four surrounding adjacent fans at the outlet of the ducts.


[1] L. F. Simons and C. Salter, Proc. Roy. Soc. Ser. A **415**, 212 (1934).
[2] G. Comte-Bellot and S. Corrsin, J. Fluid Mech. **25**, 657 (1966).
[3] P. Lavoie, L. Djenidi, and R. A. Antonia, J. Fluid Mech. **585**, 395 (2007).
[4] P.-Å. Krogstad and P. A. Davidson, J. Fluid Mech. **642**, 2009 (2010).
[5] T. Kitamura, K. Nagata, Y. Sakai, A. Sasoh, O. Terashima, H. Saito, and T. Harasaki, J. Fluid Mech. **738**, 378 (2014).
[6] L. Djenidi, Md. Kamruzzaman, and R. A. Antonia, J. Fluid Mech. **779**, 544 (2015).
[7] G. K. Batchelor, *The Theory of Homogeneous Turbulence* (Cambridge University Press, Cambridge, 1953).
[8] P. A. Davidson, *Turbulence: An Introduction for Scientists and Engineers* (Oxford University Press, Oxford, 2004).
[9] P. Sagaut and C. Cambon, *Homogeneous Turbulence Dynamics* (Cambridge University Press, Cambridge, 2008).
[10] D. Hurst and J. C. Vassilicos, Phys. Fluids **19**, 035103 (2007).
[11] R. E. Seoud and J. C. Vassilicos, Phys. Fluids **19**, 105108 (2007).
[12] H. Makita, Fluid Dyn. Res. **8**, 53 (1991).
[13] L. Mydlarski and Z. Warhaft, J. Fluid Mech. **320**, 331 (1996).
[14] R. J. Hearst and P. Lavoie, Exp. Fluids **56**, 185 (2015).
[15] R. E. G. Poorte and A. Biesheuvel, J. Fluid Mech. **461**, 127 (2002).
[16] P. Knebel and J. Peinke, Active grid generated turbulence, in *Advances in Turbulence XII*, edited by B. Eckhardt, Springer Proc. Phys. Vol. 132 (Springer, Berlin, Heidelberg, 2009), p. 903.
[17] H. E. Cekli, C. Tipton, and W. van de Water, Phys. Rev. Lett. **105**, 044503 (2010).
[18] P. Knebel, A. Kittel, and J. Peinke, Exp. Fluids **51**, 471 (2011).
[19] H. E. Cekli, R. Joosten, and W. van de Water, Phys. Fluids **27**, 125107 (2015).
[20] S. Ozono and H. Ikeda, Exp. Fluids **59**, 187 (2018).
[21] H. S. Kang, S. Chester, and C. Meneveau, J. Fluid Mech. **480**, 129 (2003).
[22] J. V. Larssen and W. J. Devenport, Exp. Fluids **50**, 1207 (2011).
[23] K. Takamure and S. Ozono, Trans. JSME **82**, 15-00575 (2016) (in Japanese).
[24] S. Ozono, H. Miyagi, and K. Wada, J. Fluid Sci. Tech. **2**, 634 (2007).
[25] S. Ozono, A. Nishi, and H. Miyagi, J. Wind Eng. Ind. Aerodyn. **94**, 225 (2006).
[26] S. Rezaeiravesh, R. Vinuesa, M. Liefvendahl, and P. Schlatter, Eur. J. Mech-B/Fluids **72**, 57 (2018).
[27] T. Gotoh and T. Watanabe, J. Turb. **6**, N33 (2005).
[28] L. P. Bernal and A. Roshko, J. Fluid Mech. **170**, 499 (1986).
[29] M. Gharib and K. Williams-Stuber, J. Fluid Mech. **208**, 225 (1989).
[30] S. Kida, M. Yamada, and K. Ohkitani, Physica D **37**, 116 (1989).